# Concave Rhombic Dodecahedral Au Nanocatalyst with Multiple High-Index Facets for CO₂ Reduction

Hye-Eun Lee,[†] Ki Dong Yang,[†] Sang Moon Yoon,[†] Hyo-Yong Ahn,[†] Yoon Young Lee,[†] Hyejin Chang,[‡] Dae Hong Jeong,[‡] Yoon-Sik Lee,[§] Mi Young Kim,[†] and Ki Tae Nam*,[†]

[†]Department of Materials Science and Engineering, and [§]School of Chemical and Biological Engineering, Seoul National University, Seoul, 151-744, Korea and [‡]Department of Chemistry Education, Seoul National University, Seoul 151-748, Korea

ABSTRACT A concave rhombic dodecahedron (RD) gold nanoparticle was synthesized by adding 4-aminothiophenol (4-ATP) during growth from seeds. This shape is enclosed by stabilized facets of various high-indexes, such as (331), (221), and (553). Because it is driven thermodynamically and stabilized by 4-ATP ligands, the concave RD maintains its structure over a few months, even after rigorous electrochemical reactions. We discussed the mechanism of the shape evolution controlled by 4-ATP and found that both the binding energy of Au—S and the aromatic geometry of 4-ATP are major determinants of Au atom deposition during growth. As a possible application, we demonstrated that the concave RD exhibits superior electrocatalytic performance for the selective conversion of CO₂ to CO in aqueous solution.
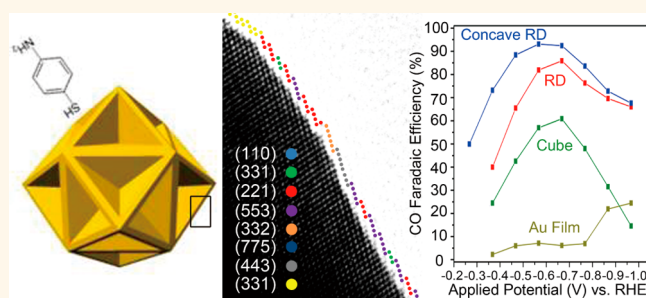
KEYWORDS: concave nanoparticle · catalyst · CO₂ reduction · high-index facet · benzenethiol · gold

Nanoparticles enclosed by high-index facets have attracted attention because of their unexpected catalytic and optical properties.[1−9] The fascinating catalytic properties of high-index facets result from the high density of atomic steps that can serve as active sites for chemical reactions. It is challenging to fabricate high-index facet as these surfaces possess higher surface energy than low-index facet. Continuous efforts to create nanoparticles with high-index surfaces has led to the development of various strategies such as etching the specific surface,[10−12] kinetically controlling the growth,[13−15] and utilizing adsorbate.[16−20] As an example of adsorbate, silver ion has been most frequently used to synthesize various high-index facets such as {720},[16] {310},[17] and {037}[18] Au nanocrystal. Methylamine and KBr were also exploited to generate different high-index facets of Pt nanoparticle with a {411}[19] and {720}[20] surface respectively by selective binding of additives on the surface. Recently, the concave RD shape was also reported using dimethylformamide

reduction.[21] Here we developed a new way to produce high-index nanoparticles by using organothiol as a shape-controlling additive. Typically organothiol has been used for fabricating a self-assembled monolayer,[22] functionalizing the nanoparticles,[23] and encoding the Raman signal[24,25] by attaching an SH molecule to the premade nanoparticle. However, in this strategy, we add organothiol with precursor in the growth solution to induce the intriguing morphology. As a result, we create a new high-index nanoparticle, a concave rhombic dodecahedron (RD).

The increasing dependence on fossil fuels has accelerated the imbalances between energy production and demand. In the concept of carbon-based energy cycles, converting carbon dioxide (CO₂) into reusable chemical feedstock is critical. In particular, the recycling of carbon monoxide (CO) could become very important for sustainability.[26,27] Among many different approaches to reconvert CO₂ into CO, electrochemical reduction of CO₂ at the expense of renewable energy is considered to be an

environmentally benign method. However, a potential for activating the inert CO_2 molecule into $CO_2^{\bullet}$ radical requires -1.9 V vs RHE, resulting in low conversion efficiency.[28] Nanostructured gold has been known to be a promising catalyst for CO_2 reduction.[28−30] In 1987, it was found that gold nanoparticles less than 5 nm have unexpected catalytic properties.[31] It was proposed that the catalytic activity of gold can be attributed to the low-coordinated gold atoms in the nanoparticles.[32] On the basis of DFT simulation and experimental evidence, it was shown that a gold surface can adsorb and stabilize the intermediates required for CO_2 reduction while also weakening the binding of CO.[33,34] Specifically, the edge site of the nanoparticle is beneficial for CO_2 reduction owing to the many atoms with low coordination number localized at the edge.[35] Recently, Sun et al. reported (211) nanowires with increased density of edge site can improve reduction kinetics of CO_2.[30]

In this study, we created an intriguing morphology featuring a concave RD by using 4-aminothiophenol as a shape modifier. The individual nanoparticles contain 24 cavities, allowing diverse curvature of the surface and high-index facets. Surprisingly, we found out that multiple types of high-index facet exist in the single concave RD nanoparticle consisted by various combination of (111) terrace and (11$\bar{1}$) step subfacets. As a result, the concave RD exhibits superior catalytic activity for CO_2 reduction compared to low-index nanoparticles.

RESULTS AND DISCUSSION

Effect of Benzenethiol as a Nanoparticle Shape Modifier and Stabilizer. The concave RD nanoparticle was prepared by using a modified seed-mediated method (Scheme 1). In the growth solution, hexadecyltrimethylammonium bromide (CTAB) and gold(III) chloride trihydrate ($HAuCl_4$) were mixed to create the $AuBr_4^-$ complex, and this complex was reduced to Au^+ by adding ascorbic acid (AA). To this typical growth solution, different kinds of benzenethiol molecules were added as shape modifiers. Another unique feature of our method is that presynthesized 45 nm size cuboctahedron Au nanoparticles were used as seeds. In the presence of benzenethiol molecules, these seeds started to grow into various shapes, directed by the involvement of Au−S bonding and the molecular interactions of these shape modifiers. A more detailed description of the relationship between the functional groups and shape change is provided in the next section. Among the shape modifying benzenethiol molecules, 4-aminothiophenol (4-ATP) produced the most astonishing nanoparticle shape.

Figure 1 presents a morphological characterization of the concave RD. The synthesized particle was first confirmed by scanning electron microscopy (SEM). The size of the particle was 120 nm and the yield of the
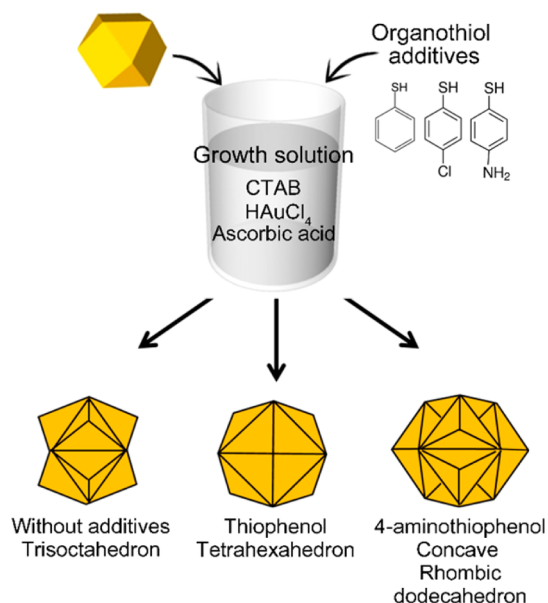
Scheme 1. Growth procedure of nanoparticle mediated by benzenethiol.

nanoparticle was about 72%. In Figure 1a, the edge parts of the nanoparticle were observed to be brighter than the inner surface of nanoparticle. This contrast difference in the SEM image indicates that the nanoparticles contain many cavities on their surfaces. With careful observation, we can see that the nanoparticle resembles the outline of a RD and has a dented surface on each facet of the RD. This structure can be more clearly understood by directly comparing a single concave RD nanoparticle (Figure 1b−d) with a RD model (Figure 1e) oriented along the same axis. In the [110] projection (Figure 1b,e), the elongated hexagon contour in the RD matches the outline of the concave RD. We can also observe characteristic hexagonal and square outlines of the RD when it is aligned with the [111] zone axis (Figure 1c) and [100] axis (Figure 1d), respectively. In contrast, the inner surface of the frame have rugged surface, which differs from a RD with a flat (110) surface. The shape of the nanoparticle also can be described as RD excavating out two trigonal pyramids from each (110) surface. To confirm this interpretation, we investigated this structure using high-angular annular dark-field scanning transmission electron microscopy (HAADF-STEM) projected along the [110] zone axis. In Figure 1f, concave features are clearly seen at the margin of particle (red arrows and marked with 1 in the model). The deep dents show decreasing intensity due to existence of fewer atoms at the concave site, and the remaining edges where higher number of atoms exist are observed with strong intensity in between the two arrows. Another characteristic of the concave surface can be found in location 2. Small triangular cavities are apparent in the STEM image, indicated by yellow arrows. The difference in location 1 and 2 are visualized in the Figure S1.
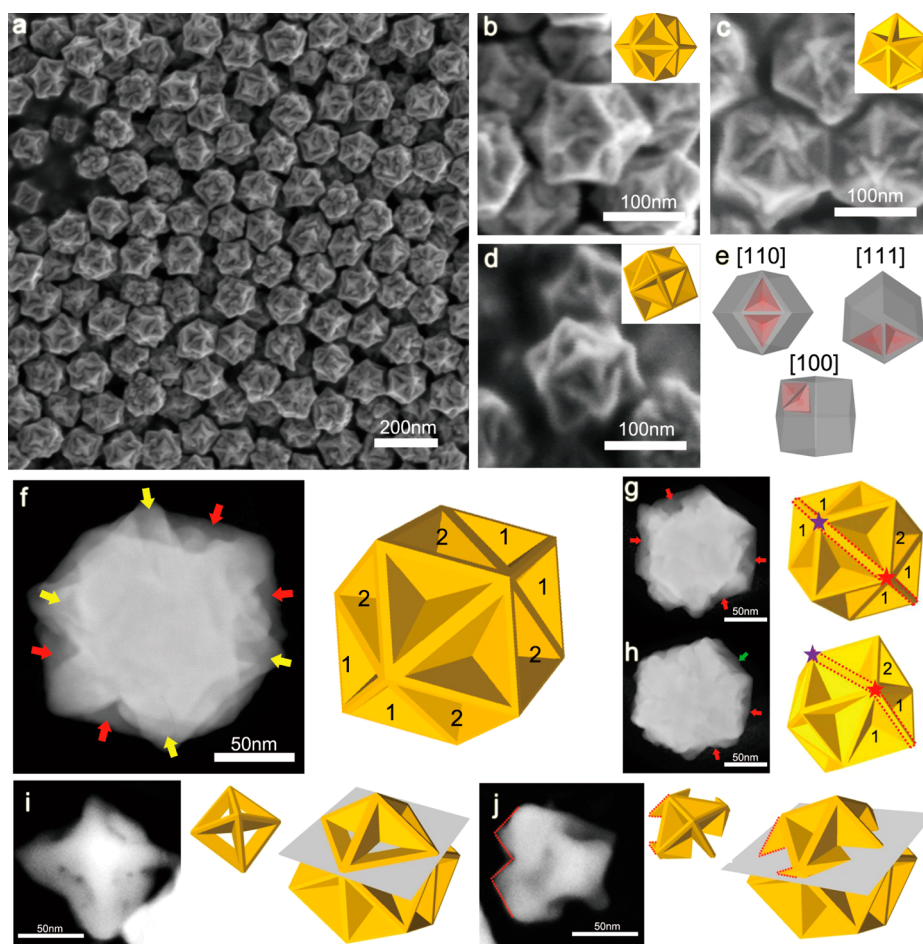
Figure 1. Morphological characterization of the concave RD. (a) Large-area SEM image of the concave RD. (b−d) High-magnification SEM images of a single nanoparticle with models projecting along (b) [110], (c) [111], and (d) [100]. (e) Illustrative model showing how the concave RD was built: two trigonal pyramids are carved out from each facet of the RD. Models are oriented with different axes [110], [111], and [100] (from left to right). (f) HAADF STEM image of a concave RD along the [110] zone axis and corresponding model. Concave parts are indicated with arrows (red, location 1 in the model; yellow, location 2 in the model). (g,h) Tilted HAADF STEM images together with the model. In panels g and h, the concave part is shown with red arrows (indicated as 1) and the newly apparent concave part is shown with a green arrow (indicated as 2) after tilting the particle by 30 degrees. (i, j) HAADF STEM images of a fragment of the concave RD obtained by cutting the top at a different angle.

The concave feature at location 2 can becomes more evident when tilted. Before tilting the nanoparticle (Figure 1g), four dented parts (red arrows) are seen from the image. When the particle is tilted by 30 degrees, two parts of site 1 at the top left disappear and site 2 emerges (green arrow), showing a cavity (Figure 1h).

To further observe the concave feature of a particle at different locations, we deliberately cut this nanoparticle by using a focused ion beam (FIB). The top of the concave RD was cut with different angles (Figure 1i,j) and analyzed by HAADF-STEM. As shown in Figure 1i, the observed cavities match perfectly with the concave RD schematics. These cavities can exist only when the surfaces are concave. The concave features can be more distinctively visualized by using a slanting cut (Figure 1j). Only one arm of the crossing line protrudes in this fragment because of height difference between the crossing line and the bottom

facet created by the concave feature. Also, the two triangles in Figure 1j (red dashed line) provide additional evidence for the dented surface of this particle. If the facet is flat, the cut end would show a single flat appearance rather than two separate triangles. On the basis of these analyses, we conclude that the concave RD was successfully synthesized.

Effect of Organothiol Structure on Nanoparticle Shape. To understand the role of benzenethiol molecules as a shape determinant, we investigated how the strength of thiol binding affects the final morphology. The synthesized nanoparticle in the absence of additives shows a trisoctahedral (TOH) shape (Figure 2a). We added *p*-phenylenediamine, which is known to interact with gold but interacts more weakly than a thiol group (Supporting Information Figure S2). The resulting nanoparticle still shows TOH morphology, indicating that a small interaction energy cannot affect the morphology. We tried three different types of
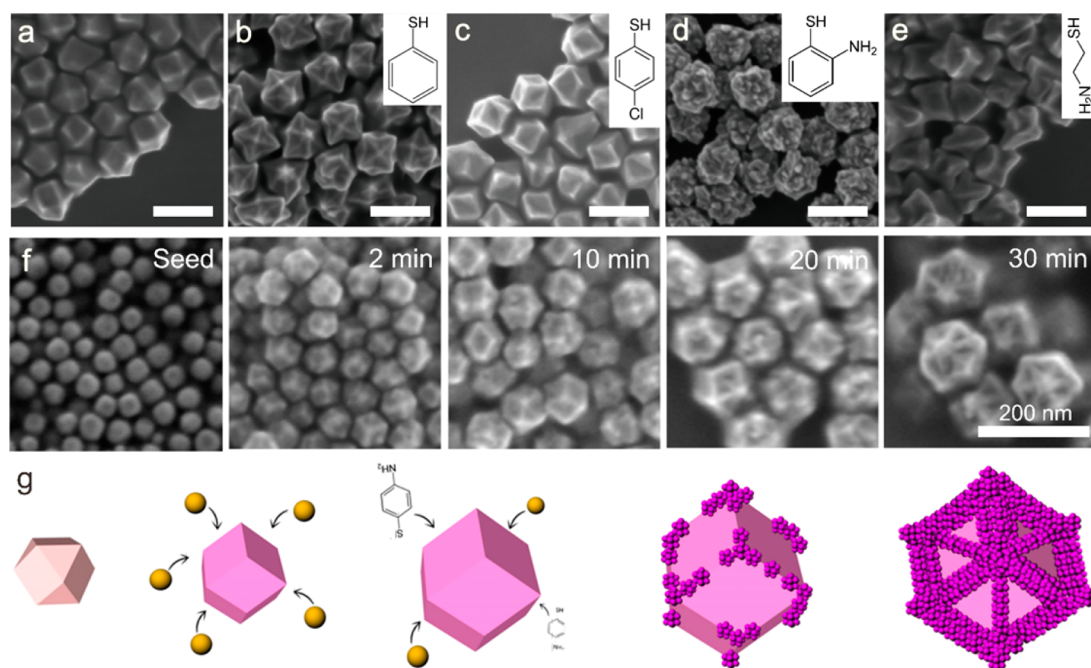
Figure 2. (a−e) Effect of organothiol on morphological change. SEM images of nanoparticles synthesized with various additives: (a) without additives, (b) thiophenol, (c) 4-chlorothiophenol, (d) 2-aminothiophenol, and (e) cysteamine. (f,g) Growth mechanism of the concave RD: (f) SEM images of the concave RD at different reaction times; (g) schematic illustration of the growth procedure. All scale bars are 200 nm.

benzenethiol 4-aminothiophenol (4-ATP), thiophenol (TP), and 4-chlorothiophenol (4-CTP) that have different functionalities at the *para* position. According to Hammett substitution theory[36] and previous simulations,[37] by changing the functional group at the *para* position, the interaction energy of the thiol group can be tuned. For the case of 4-ATP, the binding energy of thiol is significantly increased, since the amine has electron donating property. With this strong interaction energy on the gold surface, the direction of growth is significantly altered resulting in the concave surface of a nanoparticle (Figure 1). In the case of TP (Figure 2b), interaction energy is slightly decreased as only hydrogen exists instead of amine. The resultant crystal shows very different morphology, a tetrahexahedron, but it does not have dents or a concave surface due to the binding energy being lower than that of 4-ATP. In the case of 4-CTP with the electron-withdrawing chlorine, the interaction energy of thiol is dramatically reduced, and the resulting shape is similar to that made without any additives (Figure 2c). In addition to the thiol group, the position of amine is also important in the morphological evolution. When the position of amine is changed to *ortho* (2-aminothiophenol (2-ATP)), a bumpy surface is developed (Figure 2d). On the basis of scanning tunneling microscope (STM) studies, it has been known that the molecular assembly of 4-ATP and 2-ATP show different patterns on the same Au (111) surface.[38] Because of this, we think that different assembled structures of these additives on the gold surface also affect the growth. We also found that the benzene ring plays

an important role as well as the thiol group. When we add cysteamine, which has no benzene ring, irregular nanoparticle shapes are produced (Figure 2e).

Effect of Other Constituents on the Growth Solution. The concentration of each constituent in the growth solution is important for the shape evolution. In the growth solution, typical concentrations of HAuCl$_4$, AA, 4-ATP, and CTAB are 10 mM, 100 mM, 5 mM, and 100 mM, respectively. When the amount of CTAB was reduced in the growth solution (10 mM, 1 mM, and absence), the solution became turbid with the addition of HAuCl$_4$ (Supporting Information Figure S3). As the ascorbic acid is mixed into the solution (1 mM of CTAB and absence of CTAB), a purple color immediately appears, indicating formation of nanoparticles (Au^0) due to the presence of AuCl$_4^-$. In contrast, in the case of 100 mM CTAB (standard concentration), the solution stays clear, indicating the generation of Au$^+$ as a complete transition from AuCl$_4^-$ to AuBr$_4^-$. The formation of Au$^+$ is a prerequisite for fabricating well-defined nanoparticles, as the growth proceeds with spatially defined deposition of Au$^+$. Therefore, high concentrations of CTAB should be used, large enough to replace all AuCl$_4^-$ with the AuBr$_4^-$ complex. In the case of 10 mM CTAB, the synthesized particles have random morphology (Supporting Information Figure S4). It has been previously reported that large aggregates of CTAB-gold salt complexes in the growth solution produce irregular shapes.[39] In this experiment, we found that the concentration of CTAB should be higher than 100 mM to synthesize a uniform concave RD. We also decreased the concentration of AA to determine the effect of AA.

In the case of 10 mM of AA ([AA]/[HAuCl$_4$] = 3), there is no difference in the shape (Supporting Information Figure S5). Considering that at least a 1.5 ratio of ascorbic acid to gold salt is needed to complete the reduction of gold, 10 mM of AA is still large enough to reduce all gold ions. Also, when the concentration of AA is reduced to 1 mM and in the absence of AA, as expected, no reduction of Au$^+$ occurs and nanoparticles do not grow (Supporting Information Figure S6).

In previous cases, high concentrations of AA have been used as a tool to induce kinetic growth of nanoparticle fabricating high-index facet or flower-like structure.[13,15,40,41] We synthesized nanoparticles under high concentrations of AA (Supporting Information Figure S7), however, and there is no difference in the morphology of the resulting nanoparticle, even when synthesized at 0.5 M AA ([AA]/[HAuCl$_4$] = 150), which is a significantly higher concentration than previously reported ([AA]/[metal precursor] = 4 for {541} facet and [AA]/[metal precursor] = 20 for flowerlike structure).[15] This indicates that our concave structure does not originate from the kinetic control adopted before.

The concentration of 4-ATP significantly modifies the development of shape. In the case of 2 mM 4-ATP (Supporting Information Figure S8) instead of 5 mM, fewer ridges are formed in the nanoparticles. When the concentration of 4-ATP increases up to 10 mM, the final shape has more rugged surfaces and increased deposition along the [111] direction.

In summary, a concentration of CTAB higher than 100 mM and a concentration of AA greater than 10 mM should be used to create AuBr$_4^-$ and Au$^+$, respectively. Even at high concentrations of AA (500 mM), the obtained morphology shows no difference from the 10 mM AA case. In contrast, small changes in the concentration of 4-ATP (from 2 mM to 10 mM) significantly modify the shape of the resulting crystal. In the conventional method used to create high-index nanoparticles, a high concentration of AA is used to create kinetic growth by increasing the reaction rate. Our concave RD, however, is invariant even under a 50-fold difference in AA concentration, but the concentration of 4-ATP significantly affects to the shape. These results suggest that a concave RD is derived only by 4-ATP-induced changes and not by any kinetic growth.

Proposed Growth Mechanism. For more detailed observation of the growth mechanism of concave RD, we monitored the growth of the concave RD as a function of time (Figure 2f). To terminate the reaction, we collected samples at different times and centrifuged them to wash out unreacted agents. Within 2 min, the cuboctahedron nanoparticle changed to a RD, and the RD continued to grow for 10 min, at which point it had a size of 80 nm. From 10 to 20 min, the projected edges start to emerge, and after 30 min, the concave features become prominent because growth occurred only at

the edge. Figure 2g schematically illustrates the growth model of the concave RD. On the basis of the morphological transition, the growth process can be divided into three stages. For RD shapes that have a high energy, the {110} facet is formed at the initial stage (t = 2−10 min) of growth. Considering the ratio of HAuCl$_4$ and 4-ATP (HAuCl$_4$:4-ATP = 200:1), it is presumed that many Au atoms are immediately attached to the seed nanoparticle before 4-ATP is attached to the particle, and this creates the RD because of the high concentration of HAuCl$_4$ at the initial stage. It was reported that increasing the concentration of Au precursor results in higher supersaturation and forms nanoparticle with higher surface energy.[14] We also compared the early stage of nanoparticle growth when TP and 2-ATP was used as an additive instead of 4-ATP. Surprisingly, in both cases, early stage morphology was RD, suggesting that the additive starts to play a major role after the formation of the RD shape (Supporting Information Figure S9).

During the second stage of growth (t = 10−20 min), the nanoparticle continues to grow, and the edge of the nanoparticle starts to protrude. To determine how 4-ATP interacts with the nanoparticles and directs their shape evolution, we varied the injection sequence of 4-ATP. When cuboctahedron seeds were treated with 4-ATP molecules before being added to the growth solution, the resulting particles exhibited irregular morphologies. In contrast, when 4-ATP-treated RD was used as a seed, the contour of the RD was found at some spots (Supporting Information Figure S10). From this experiment, three explanations for mechanism can be inferred. First, the point where 4-ATP molecules adhere is the time after the frame of RD is fully formed from the evidence that the outline of a RD is only observed in the RD seed case. Second, the 4-ATP molecules are gradually attached as the growth proceeds rather than being immediately attached to the surface. Third, the 4-ATP may assemble on the surface of the concave RD. The evidence shows that the 4-ATP attached RD case, where 4-ATP molecules are randomly deposited with preexisting CTAB, only leads to rougher nanoparticles. In the third stage (t = 30 min), the concave surface starts to appear as the growth of edges become dominant. Because flat surfaces were covered by the assembled 4-ATP, gold atoms deposit preferentially onto the loosely covered edge.

Surface Facet Crystallographic Analysis. The surface structure of concave RD was further examined by high-resolution transmission electron microscopy (TEM). Figure 3a shows representative TEM images of concave RD oriented with the [110] axis. The atomic arrangement of a concave RD can be directly seen when viewed along the [110] direction. As clearly shown in the Figure 3 section A-1 to C-3, many of the terraces and steps are directly observed in the projected atom images. According to the microfacet nomenclature,[42] a
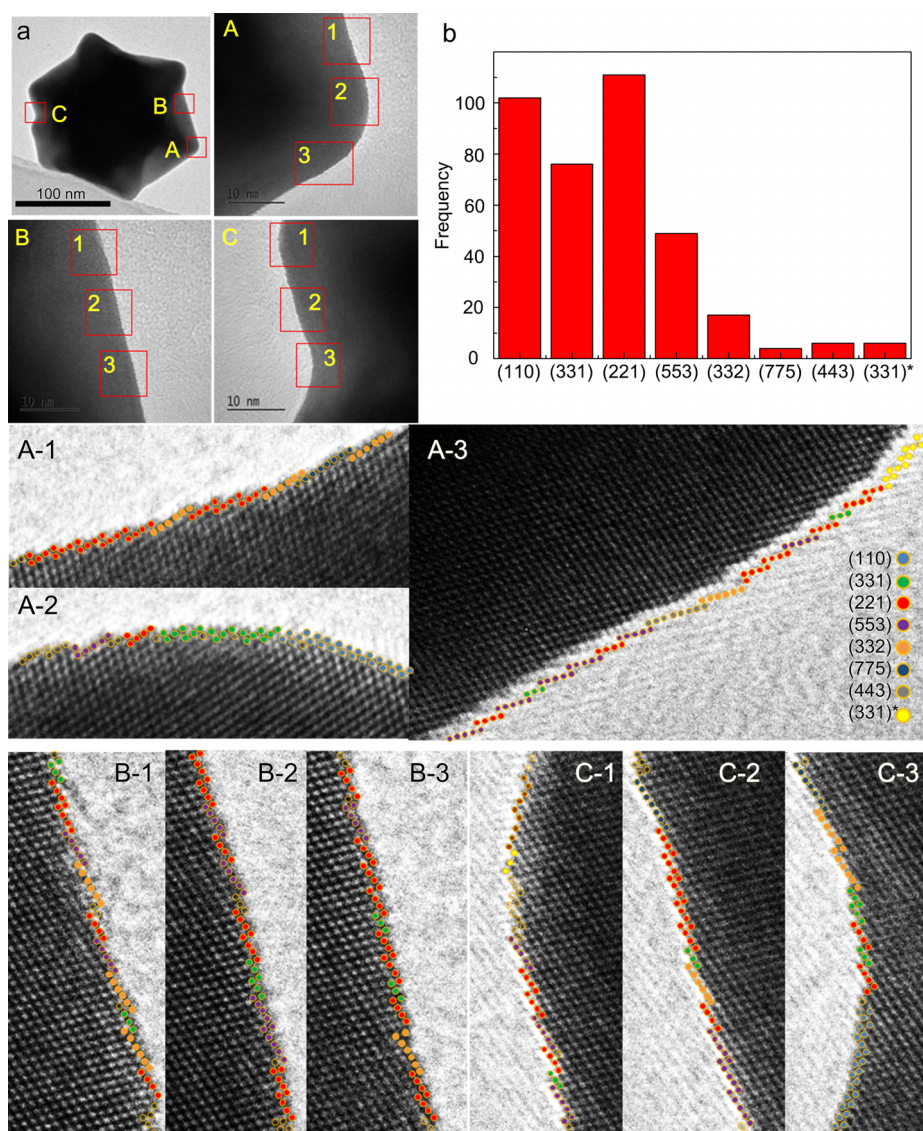
Figure 3. Atomic structures of the RD. (a) TEM images of individual concave RDs viewed along the [110] direction, and magnified images of a concave RD at the vertex (A), edge (B), and bump (C). Each different part is subdivided by three sections. (A-1 to C-3) HRTEM images of nine different sections displaying atomic arrangements. Each atom is marked with a colored sphere. Different colors were assigned to each type of facet (various terrace units from (110) $[(^1/_2)_1 (111) + (^1/_2)_1 (11\bar{1})]$ to (443) $[(^7/_2)_7 (111) + (^1/_2)_1 (11\bar{1})]$, and different types of (331) $[2_1 (110) + 1_1 (111)]$ surface, which is denoted by an asterisk, were identified). The indexes of these colors are shown in section A-3. (b) Histogram of facets that consist of concave RDs. N = 371.

high-index facet can be characterized by a combination of low-index subfacets. For instance, the microstructure of (331) can be divided into two units of (111) terrace and one unit of $(11\bar{1})$ step. We carefully examine the composition of subfacets in the surface to determine the index of the surface. Three different parts in the nanoparticle, vertex (A), edge (B), and bump (C) are carefully examined. Each part is subdivided by three sections depending on the curvature. Interestingly, the nine different surfaces are terminated with various types of steps and terraces according to local curvature. To clarify the position of the surface atoms, each atom is marked with a colored sphere. In the case of section A-1, there is an elevated inclination of surface at the right side, and the increased slope

comes from the higher index of a facet like (332) $(^5/_2)_5$ $(111) + (^1/_2)_1 (11\bar{1})$ and (775) $[6_6 (111) + 1_1(11\bar{1})]$. In contrast, for the highest positive degree of curvature (section A-2), the surface mainly consists of a relatively low-index terrace unit such as (110), (331), and (221) to minimize surface tension. For section A-3 case where various degree of inclination exists, even seven different types of facet are founded within 15 nm distance. Though in the location B there is not much change in the gradient, different high facets like (331), (221), (553), and (332) are alternately observed. In location C, where positive and negative curvature with various gradients constitutes the surface, the highest number of types of high-index facets is observed. The distribution of diverse high-index facets was analyzed and

displayed in a histogram. The facets of (110), (331), (221), and (553) were found most frequently (N = 371). In the concave RD, assorted facets with various terrace units from (110) [($^1/_2$)$_1$ (111) + ($^1/_2$)$_1$ (11$\overline{1}$)] to (443) [($^7/_2$)$_7$ (111) + ($^1/_2$)$_1$ (11$\overline{1}$)] were observed, and a different type of (331) surface consisting of (110) terrace and (111) step was also discovered.

Electrocatalytic Performance for CO$_2$ Reduction. To evaluate the concave RD as an electrocatalyst for CO$_2$ conversion, cyclic voltammetry (CV) measurements were conducted in CO$_2$-purged 0.5 M KHCO$_3$ (pH 7.3). The electrode was prepared by the conventional drop-casting method of Au nanoparticles on carbon paper. As shown in Figure S11, the chemical selectivity of the electrodes was affected by the amount of loaded Au nanoparticles (see Supporting Information for calculation of loading amount). To avoid this effect, the number of drops was kept constant on the carbon paper, and a controlled size was used. To compare the catalytic activity of each Au nanoparticle (concave RD, RD, cube, and Au film, Supporting Information Figure S12), the potential to attain catalytic current density of 0.15 mA/cm^2 was defined as an onset potential. The current density is normalized to the area of working electrode. On an Au film electrode, as shown in Figure 4a, the current density increases gradually from −0.42 V vs RHE and reaches 6.4 mA/cm^2 at −1.2 V vs RHE as the potential is negatively applied. As the carbon paper is decorated with a RD Au nanoparticle, the onset potential is positively shifted by 0.22 V, while it is anodically shifted by 0.1 V in the case of a cube Au nanoparticle. This implies that the exposed facets on the Au nanoparticles can affect the electrocatalytic activities for CO$_2$ reduction. Indeed, the overall J−E curve is much more positively shifted by 0.21 V compared to that of Au film, when the electrode is decorated with concave RDs. Among Au nanoparticles, a concave RD exhibits the lowest onset potential at −0.23 V vs RHE with the current density increasing up to 10.6 mA/cm^2 at −1.2 V vs RHE which is 1.2 times higher than that of Au film. Compared to previously reported polycrystalline Au nanoparticles, the onset potential is reduced by approximately 0.18 V.[35] This result demonstrates that the electrocatalytic reduction of CO$_2$ can be facilitated by introducing more facets on the Au nanoparticles. However, it is also known that the current density measured in the solution saturated with CO$_2$ is attributable to both CO$_2$ reduction and a hydrogen evolution reaction (HER).[29] Therefore, the effluent gas from the Au nanoparticle-dropped electrode was subjected to gas chromatography (GC), which can analyze CO, H$_2$, CH$_4$, and C$_2$H$_4$.

The GC analysis shows that the catalytic reduction of CO$_2$ is strongly shape-dependent, and the concave RD exhibits the most outstanding performance for CO formation. The Au nanoparticles yielded CO as a major product. Minor products detected by gas
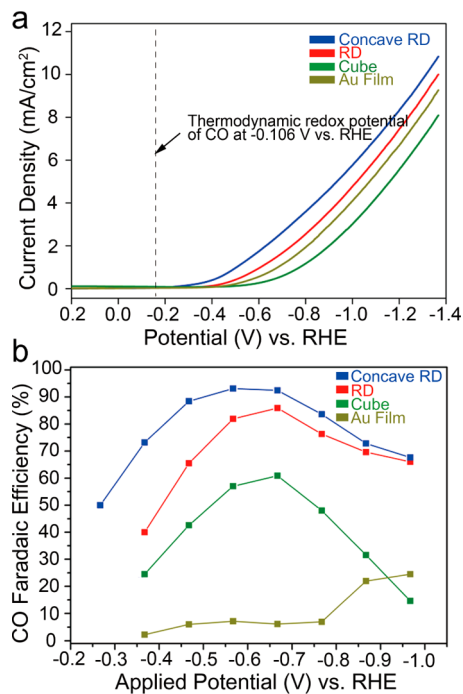

Figure 4. Electrochemical performance of the concave RD. (a) Cyclic voltammetry curves of carbon paper decorated with concave RD (blue), RD Au NP (red), cube Au NP (green) and Au film (olive) (b) Faradaic efficiency for CO vs applied potential of Au film and Au nanoparticles. All electrolysis experiments were conducted at −1.0 V vs RHE.

chromatography and NMR are H$_2$, HCOOH, and CH$_4$ (Supporting Information Table S1). As shown in Figure 4b, the breadths of faradaic efficiency for CO against applied potential curves of concave RD were broad compared with the RD and cube nanoparticles. The RD exhibits approximately 41% faradaic efficiency at −0.37 V vs RHE, and an even lower selectivity of 24% is shown from cube. The saturated faradaic efficiencies of both particles are also positioned far below that of the concave RD, achieving 86% (RD) and 61% (cube). In addition, the Au film exclusively produced H$_2$ at low applied potential, and a small amount of CO was detected above −0.8 V vs RHE. Additionally, in the case of the concave RD, approximately 52% of the CO is generated at a potential of −0.26 V vs RHE which is 0.14 V lower than the theoretical equilibrium potential (−0.11 V vs RHE). As the higher potential is applied, faradaic efficiency for CO arises gradually and almost reaches saturation at −0.57 V vs RHE, exhibiting 93% of CO selectivity. In particular, a significant change in the faradaic efficiency of CO is observed on concave RD at −0.37 V vs RHE, producing 73% of CO which is approximately 3 times higher than that of Au nanoparticle exposed with low-index facet. Compared with the previously reported polycrystalline Au nanoparticle, the chemical selectivity from the concave RD is remarkable. It is known that polycrystalline Au nanoparticles catalyze CO$_2$ into CO with faradaic efficiency of 90% at −0.67 V vs RHE, while the selectivity is dramatically

decreased to less than 20% at −0.37 V *vs* RHE.[43,44] On the basis of the faradaic efficiency confirmed by GC, the mass activity of each Au nanoparticle also can be calculated to compare the catalytic performance per unit mass (Supporting Information Figure S13). Compared with RD and Cube, concave RD still exhibits much higher activity for CO formation. Therefore, the high faradaic efficiency observed for the concave RD is noteworthy in the aspects of both the onset potential and the chemical selectivity.

Taken together, the CV analysis and GC results provide insights into the effects of a high number of facets on CO_2 reduction. Recently, energetics for CO_2 reduction depending on Au facet was computationally simulated for (111) and (211) plane in an fcc structure, suggesting (211) as the origin of the enhanced catalytic activity.[34,35] Similarly, it was empirically proven that the (110) plane exhibits the highest electrocatalytic activity for CO evolution followed by (111) and (100) on an Ag electrode.[45] This provides a clue for understanding the tendency toward CO evolution observed for RD (covered with (110)) and Cube (covered with (100)). However, the catalytic reduction of CO_2 on a much higher index has not been shown. Interestingly, concave RD is enclosed with high-index of facet such as (332) and (775). This indicates that a higher-facet index can introduce a favorable route for CO_2 reduction.

To verify the stability of the Au nanoparticle during the CO_2 reducing reaction, bulk electrolysis was conducted for 30000 s. As shown in the Figure S14, all three types of nanoparticles dropped on the carbon paper exhibit consistent current density, demonstrating high stability of the synthesized nanoparticle. After the electrolysis, the concave features of the concave RD are still maintained as confirmed by SEM (Supporting Information Figure S15).

CONCLUSION

We synthesized a concave RD by using 4-aminothiophenol as an additive. We found that changing the binding energy of Au−S and the functional group in benzenethiol induces dramatic morphology changes, because these benzenethiol additives are gradually incorporated into the nanoparticle and modify the growth pathway of the Au atoms during the growth of the nanoparticle. The single concave RD possesses multiple high-index facets, which are terminated by numerous atomic steps. Eight different types of high-index facets were recognized in an individual concave RD, and (110), (331), (221), and (553) were observed most frequently. As a consequence of the high density of atomic steps on the surface, the concave RD exhibits enhanced catalytic activity compared to low-index nanoparticles. Moreover, this concave RD shows superior stability for long-term electrocatalytic performance. This new methodology and novel morphology will open up new possibilities for not only synthesizing intriguing morphology, but also fabricating various catalysts.

EXPERIMENTAL METHODS

Chemicals. Hexadecyltrimethylammonium bromide (CTAB, 99%), L-ascorbic acid (AA, 99%), and tetrachloroauric (III) trihydrate ($HAuCl_4 \cdot 3H_2O$, 99.9%) were purchased from Sigma-Aldrich. 4-Aminothiophenol (4-ATP, 98.0%, TCI), 4-chlorothiophenol (4-CTP, 98%, Acros), thiophenol (TP, 99%, Sigma-Aldrich), 2-aminothiophenol (2-ATP, 95%, TCI), and cysteamine (98%, Acros) were used without further purification. Dimethyl sulfoxide (DMSO, 99.5%) was obtained from Daejung Chemicals. All aqueous solutions were prepared using high-purity deionized water (18.2 MΩ/cm).

Synthesis of Seed. Cuboctahedra with a size of 45 nm were synthesized as previously reported.[41] Briefly, small seeds (∼2.5 nm) were first created by rapid reduction of $HAuCl_4$ (10 mM, 0.25 mL) using a strong reductant, sodium borohydride (10 mM, 0.8 mL), under a CTAB environment (100 mM, 7.5 mL). After it was added to the growth solution which contains $HAuCl_4$ (10 mM, 0.2 mL), CTAB (100 mM, 1.6 mL), and AA (50 mM, 0.95 mL), the small seed was further grown to a 45 nm cuboctahedron shape within 15 min. The synthesized nanoparticles were washed twice by centrifugation (10000 rpm, 1 min) and dispersed in DIW for further use.

Synthesis of Concave RD. In a typical synthesis, 0.8 mL of 100 mM CTAB was added to 3.95 mL of DIW. Au precursor (10 mM, 0.1 mL), AA (0.1 M, 0.475 mL), and 4-ATP (5 mM, 0.5 μL) were mixed into the solution consecutively. 4-ATP was dissolved in DMSO while all other chemicals were prepared in DIW. The growth of the concave RD was started as with the addition of the cuboctahedron seed that was previously made. The solution was left for 2 h in the 30 °C bath. The pink solution originated from a 45 nm seed and gradually became purple with a large scattering color within 30 min. The solution was centrifuged twice (5000 rpm, 40 s) to remove unreacted reagents.

Characterization. A Zeiss Supra 55 VP (Zeiss, Oberkochen, Germany) instrument was used for scanning electron microscopy (SEM). A JEM 2100F (JEOL, Tokyo, Japan) transmission electron microscope was used to acquire HR-TEM and HADDF-STEM images, operating at 200 kV. Samples were prepared by dropping gold nanoparticle solutions onto a silicon wafer or carbon support film grid for SEM and TEM, respectively. The remaining solution was wicked out by using filter paper and dried at room temperature. For dissection of the nanoparticle, a FEI Helios 650 FIB instrument was used.

Electrode Preparation. Two hundred microliters of concave RD solution (7×10^{10}/mL) dropped onto the 0.5 cm × 1 cm carbon paper. The solvent on the carbon paper was removed by a vacuum pump. The carbon paper deposited with gold nanoparticle was washed with ethanol to remove the remaining CTAB and was used as a working electrode. Electrodes decorated with cube and RD were also prepared in the same way. Cube and RD nanoparticles enclosed by the (100) surface and (110) surface respectively were synthesized by following the previously reported method.[41] For a gold film electrode where the (111) surface mainly exist, Au was sputtered on the carbon paper, and annealing was performed at 300 °C for 5 h.

Electrochemical Methods. All electrochemical measurements were performed in a three-electrode electrochemical cell system (Supporting Information Scheme S1). An ALS Ag/AgCl reference electrode (in 3 M NaCl and 0.01 M $AgNO_3$) and Pt foil (2 cm × 2 cm × 0.1 mm, 99.997% purity, Alfa Aesar) were used as the reference electrode and counter electrode, respectively. The applied potential of carbon paper with Au nanoparticles was controlled using a potentiostat system (CHI 760E,

CH Instruments, Inc.) at ambient temperature (21 ± 1 °C). The potential of the Ag/AgCl reference electrode has a relationship with the RHE: RHE = E(Ag/AgCl/3 M NaCl) + 0.197 + (0.591 × pH) V. In addition, iR compensation was performed by the using following equation ($V = V_{applied} - iR$). The electrolyte in all experiments was 0.5 M $KHCO_3$ unless otherwise noted. The electrolyte was degassed by bubbling with high-purity argon (99.999%) before the start of each experiment, and then it was purged with high-purity CO_2 (99.999%) for at least 30 min.

Gas Chromatography. The products were quantitatively analyzed by using flame ionization detector gas chromatography (FID-GC, PerkinElmer, NARL8502 model 4003) equipped with an active-carbon-packed column (6′ HayeSep N 60/80 SF, carrier gas: Ar) at 120 °C. The evolved gas in the head space of the reactor was injected into the FID-GC with a volume of 1 mL. The molar proportion of the products was relatively measured. The exact amount of gas was calculated by multiplying the volume by the volume of the head space. The number of moles of CO evolved during electrolysis was calculated from the integrated area of the CO peak in the gas chromatogram using 0.1 mol % of CO as a standard gas. The Faradaic efficiency for the electroreduction of CO_2 was measured by running a controlled potential electrolysis without stirring and iR compensation.

Conflict of Interest: The authors declare no competing financial interest.

REFERENCES AND NOTES

1. Zhang, L.; Niu, W.; Xu, G. Synthesis and Applications of Noble Metal Nanocrystals with High-Energy Facets. *Nano Today* **2012**, *7*, 586–605.
2. Quan, Z.; Wang, Y.; Fang, J. High-Index Faceted Noble Metal Nanocrystals. *Acc. Chem. Res.* **2013**, *46*, 191–202.
3. Zhang, Q.; Wang, H. Facet-Dependent Catalytic Activities of Au Nanoparticles Enclosed by High-Index Facets. *ACS Catal.* **2014**, *4*, 4027–4033.
4. Xia, X.; Zeng, J.; McDearmon, B.; Zheng, Y.; Li, Q.; Xia, Y. Silver Nanocrystals with Concave Surfaces and Their Optical and Surface-Enhanced Raman Scattering Properties. *Angew. Chem., Int. Ed.* **2011**, *50*, 12542–12546.
5. Zhang, Z. C.; Hui, J. F.; Liu, Z. C.; Zhang, X.; Zhuang, J.; Wang, X. Glycine-Mediated Syntheses of Pt Concave Nanocubes with High-Index {hk0} Facets and Their Enhanced Electrocatalytic Activities. *Langmuir* **2012**, *28*, 14845–14848.
6. Zhu, Z.; Meng, H.; Liu, W.; Liu, X.; Gong, J.; Qiu, X.; Jiang, L.; Wang, D.; Tang, Z. Superstructures and SERS Properties of Gold Nanocrystals with Different Shapes. *Angew. Chem., Int. Ed.* **2011**, *50*, 1593–1596.
7. Wang, J.; Gong, J.; Xiong, Y.; Yang, J.; Gao, Y.; Liu, Y.; Lu, X.; Tang, Z. Shape-Dependent Electrocatalytic Activity of Monodispersed Gold Nanocrystals toward Glucose Oxidation. *Chem. Commun.* **2011**, *47*, 6894–6896.
8. Hong, J. W.; Lee, S. U.; Lee, Y. W.; Han, S. W. Hexoctahedral Au Nanocrystals with High-Index Facets and Their Optical and Surface-Enhanced Raman Scattering Properties. *J. Am. Chem. Soc.* **2012**, *134*, 4565–4568.
9. Kim, D.; Lee, Y. W.; Lee, S. B.; Han, S. W. Convex Polyhedral Au@Pd Core-Shell Nanocrystals with High-Index Facets. *Angew. Chem., Int. Ed.* **2012**, *51*, 159–163.
10. Jing, H.; Zhang, Q.; Large, N.; Yu, C.; Blom, D. A.; Nordlander, P.; Wang, H. Tunable Plasmonic Nanoparticles with Catalytically Active High-Index Facets. *Nano Lett.* **2014**, *14*, 3674–3682.
11. Zhang, Z. C.; Nosheen, F.; Zhang, J. C.; Yang, Y.; Wang, P. P.; Zhuang, J.; Wang, X. Growth of Concave Polyhedral Pd Nanocrystals with 32 Facets Through *In Situ* Facet-Selective Etching. *ChemSusChem* **2013**, *6*, 1893–1897.
12. Zhang, H.; Jin, M.; Wang, J.; Li, W.; Camargo, P. H.; Kim, M. J.; Yang, D.; Xie, Z.; Xia, Y. Synthesis of Pd-Pt Bimetallic Nanocrystals with a Concave Structure through a Bromide-Induced Galvanic Replacement Reaction. *J. Am. Chem. Soc.* **2011**, *133*, 6078–6089.
13. Zhang, L.; Niu, W.; Gao, W.; Qi, L.; Lai, J.; Zhao, J.; Xu, G. Synthesis of Convex Hexoctahedral Palladium@Gold Core-Shell Nanocrystals with {431} High-Index Facets with Remarkable Electrochemiluminescence Activities. *ACS Nano* **2014**, *8*, 5953–5958.
14. Lin, H. X.; Lei, Z. C.; Jiang, Z. Y.; Hou, C. P.; Liu, D. Y.; Xu, M. M.; Tian, Z. Q.; Xie, Z. X. Supersaturation-Dependent Surface Structure Evolution: From Ionic, Molecular to Metallic Micro/Nanocrystals. *J. Am. Chem. Soc.* **2013**, *135*, 9311–9314.
15. Lee, Y. W.; Kim, D.; Hong, J. W.; Kang, S. W.; Lee, S. B.; Han, S. W. Kinetically Controlled Growth of Polyhedral Bimetallic Alloy Nanocrystals Exclusively Bound by High-Index Facets: Au-Pd Hexoctahedra. *Small* **2013**, *9*, 660–665.
16. Zhang, J.; Langille, M. R.; Personick, M. L.; Zhang, K.; Li, S.; Mirkin, C. A. Concave Cubic Gold Nanocrystals with High-Index Facets. *J. Am. Chem. Soc.* **2010**, *132*, 14012–14014.
17. Lu, F.; Zhang, Y.; Zhang, L.; Zhang, Y.; Wang, J. X.; Adzic, R. R.; Stach, E. A.; Gang, O. Truncated Ditetragonal Gold Prisms as Nanofacet Activators of Catalytic Platinum. *J. Am. Chem. Soc.* **2011**, *133*, 18074–18077.
18. Ming, T.; Feng, W.; Tang, Q.; Wang, F.; Sun, L.; Wang, J.; Yan, C. Growth of Tetrahexahedral Gold Nanocrystals with High-Index Facets. *J. Am. Chem. Soc.* **2009**, *131*, 16350–16351.
19. Huang, X.; Zhao, Z.; Fan, J.; Tan, Y.; Zheng, N. Amine-Assisted Synthesis of Concave Polyhedral Platinum Nanocrystals having {411} High-Index Facets. *J. Am. Chem. Soc.* **2011**, *133*, 4718–4721.
20. Yu, T.; Kim, D. Y.; Zhang, H.; Xia, Y. Platinum Concave Nanocubes with High-Index Facets and Their Enhanced Activity for Oxygen Reduction Reaction. *Angew. Chem., Int. Ed.* **2011**, *50*, 2773–2777.
21. You, Q.; Liu, T.; Zhao, J.; Jiang, P. Synthesis of Rhombic Dodecahedral Gold Nanocrystals by Dimethylformamide Reduction. *J. Nanosci. Nanotechnol.* **2013**, *13*, 1222–1225.
22. Love, J. C.; Estroff, L. A.; Kriebel, J. K.; Nuzzo, R. G.; Whitesides, G. M. Self-Assembled Monolayers of Thiolates on Metals as a Form of Nanotechnology. *Chem. Rev.* **2005**, *105*, 1103–1169.
23. Sperling, R. A.; Parak, W. J. Surface Modification, Functionalization and Bioconjugation of Colloidal Inorganic Nanoparticles. *Philos. Trans. R. Soc., A* **2010**, *368*, 1333–1383.
24. Wang, Y.; Yan, B.; Chen, L. SERS Tags: Novel Optical Nanoprobes for Bioanalysis. *Chem. Rev.* **2013**, *113*, 1391–1428.
25. Lee, H.-E.; Lee, H. K.; Chang, H.; Ahn, H.-Y.; Erdene, N.; Lee, H.-Y.; Lee, Y.-S.; Jeong, D. H.; Chung, J.; Nam, K. T. Virus Templated Gold Nanocube Chain for SERS Nanoprobe. *Small* **2014**, *10*, 3007–3011.
26. Kumar, B.; Llorente, M.; Froehlich, J.; Dang, T.; Sathrum, A.; Kubiak, C. P. Photochemical and Photoelectrochemical Reduction of CO_2. *Annu. Rev. Phys. Chem.* **2012**, *63*, 541–569.
27. Li, C. W.; Kanan, M. W. CO_2 Reduction at Low Overpotential on Cu Electrodes Resulting from the Reduction of Thick Cu_2O Films. *J. Am. Chem. Soc.* **2012**, *134*, 7231–7234.
28. Hori, Y., Electrochemical CO_2 Reduction on Metal Electrodes. In *Modern Aspects of Electrochemistry*; Vayenas, C. G., White, R. E., Gamboa-Aldeco, M. E., Eds.; Springer: New York, 2008; pp 89−189.
29. Koh, J. H.; Jeon, H. S.; Jee, M. S.; Nursanto, E. B.; Lee, H.; Hwang, Y. J.; Min, B. K. Oxygen Plasma Induced Hierarchically Structured Gold Electrocatalyst for Selective Reduction of Carbon Dioxide to Carbon Monoxide. *J. Phys. Chem. C* **2015**, *119*, 883–889.
30. Zhu, W.; Zhang, Y. J.; Zhang, H.; Lv, H.; Li, Q.; Michalsky, R.; Peterson, A. A.; Sun, S. Active and Selective Conversion of

CO$_2$ to CO on Ultrathin Au Nanowires. *J. Am. Chem. Soc.* **2014**, *136*, 16132–16135.

31. Haruta, M.; Kobayashi, T.; Sano, H.; Yamada, N. Novel Gold Catalysts for the Oxidation of Carbon Monoxide at a Temperature far Below 0°C. *Chem. Lett.* **1987**, *16*, 405–408.

32. Hvolbæk, B.; Janssens, T. V. W.; Clausen, B. S.; Falsig, H.; Christensen, C. H.; Nørskov, J. K. Catalytic Activity of Au Nanoparticles. *Nano Today* **2007**, *2*, 14–18.

33. Hansen, H. A.; Varley, J. B.; Peterson, A. A.; Nørskov, J. K. Understanding Trends in the Electrocatalytic Activity of Metals and Enzymes for CO$_2$ Reduction to CO. *J. Phys. Chem. Lett.* **2013**, *4*, 388–392.

34. Peterson, A. A.; Nørskov, J. K. Activity Descriptors for CO$_2$ Electroreduction to Methane on Transition-Metal Catalysts. *J. Phys. Chem. Lett.* **2012**, *3*, 251–258.

35. Zhu, W.; Michalsky, R.; Metin, O.; Lv, H.; Guo, S.; Wright, C. J.; Sun, X.; Peterson, A. A.; Sun, S. Monodisperse Au Nanoparticles for Selective Electrocatalytic Reduction of CO$_2$ to CO. *J. Am. Chem. Soc.* **2013**, *135*, 16833–16836.

36. Hammett, L. P. The Effect of Structure Upon the Reactions of Organic Compounds Benzene Derivatives. *J. Am. Chem. Soc.* **1937**, *59*, 96–103.

37. Miranda-Rojas, S.; Munoz-Castro, A.; Arratia-Perez, R.; Mendizabal, F. Theoretical Insights into the Adsorption of Neutral, Radical and Anionic Thiophenols on Gold(111). *Phys. Chem. Chem. Phys.* **2013**, *15*, 20363–20370.

38. Batz, V.; Schneeweiss, M. A.; Kramer, D.; Hagenstrom, H.; Kolb, D. M.; Mandler, D. Electrochemistry and Structure of the Isomers of Aminothiophenol Adsorbed on Gold. *J. Electroanal. Chem.* **2000**, *491*, 55–68.

39. Yan, Y.; Pillai, P. P.; Timonen, J. V.; Emami, F. S.; Vahid, A.; Grzybowski, B. A. Synthesis of Toroidal Gold Nanoparticles Assisted by Soft Templates. *Langmuir* **2014**, *30*, 9886–9890.

40. Langille, M. R.; Personick, M. L.; Zhang, J.; Mirkin, C. A. Defining Rules for the Shape Evolution of Gold Nanoparticles. *J. Am. Chem. Soc.* **2012**, *134*, 14542–14554.

41. Ahn, H.-Y.; Lee, H.-E.; Jin, K.; Nam, K. T. Extended Gold Nano-Morphology Diagram: Synthesis of Rhombic Dodecahedra using CTAB and Ascorbic Acid. *J. Mater. Chem. C* **2013**, *1*, 6861–6868.

42. Van Hove, M. A.; Somorjai, G. A. A New Microfacet Notation for High-Miller-Index Surfaces of Cubic Materials with Terrace, Step and Kink Structures. *Surf. Sci.* **1980**, *92*, 489–518.

43. Hori, Y.; Murata, A.; Kikuchi, K.; Suzuki, S. Electrochemical Reduction of Carbon Dioxide to Carbon Monoxide at a Gold Electrode in Aqueous Potassium Hydrogen Carbonate. *J. Chem. Soc., Chem. Commun.* **1987**, 728–729.

44. Chen, Y.; Li, C. W.; Kanan, M. W. Aqueous CO$_2$ Reduction at Very Low Overpotential on Oxide-Derived Au Nanoparticles. *J. Am. Chem. Soc.* **2012**, *134*, 19969–19972.

45. Lu, Q.; Rosen, J.; Zhou, Y.; Hutchings, G. S.; Kimmel, Y. C.; Chen, J. G.; Jiao, F. A Selective and Efficient Electrocatalyst for Carbon Dioxide Reduction. *Nat. Commun.* **2014**, *5*, 3242.